

## Electronic supplementary information

### **Atmospheric water harvesters-assisted solar steam generation for highly efficient collection of distilled water**

*Suwei Dong, Yunfan Xu, Chenjie Wang, Cihui Liu, Jinlei Zhang, Yunsong Di, Liyan Yu, Lifeng Dong, and Zhixing Gan\**

#### **1. Supplementary Methods**

##### **1.1 The preparation of RGO slurry and CLP-LiCl AWH.**

*Preparation of RGO slurry:* GO powder was reduced to RGO by a hydrothermal method. First, 500 mg GO was put into 50 ml deionized water to prepare a 10 mg/ml suspension, and the mixture was stirred uniformly by ultrasonic. The prepared GO suspension was put into a hydrothermal autoclave and heated at 200 °C for 10 hours. The RGO slurry was obtained by mixing the RGO powder and resin solution at a mass ratio of 1:10.

*Preparation of the columnar RGO bundles:* RGO films were fabricated by coating the RGO slurry on the edges of the filter papers. Then the RGO films were rolled into cylindrical scrolls. The length of the RGO part for all the scrolls kept about 3 cm (see more details in Figure S16), the scrolls were assembled into bundles by tying. The RGO coating amounts were about 0.23 and 0.25 g for the scrolls with radii of 2.75 and 2.25 mm, respectively.

*Preparation of CLP-LiCl AWH:* Carbonized loofah powder was obtained by thermal calcination of loofah at 400 °C for 2 hours. Then, NIPAM (56.7 mg) was mixed with 1 ml deionized water to prepare a NIPAM solution, and carbonized loofah powder was added under ultrasonic treatment. 4-Methylpropiophenone (7 µL) was added as a photo initiator under an ice bath in dark. A hydrogel was obtained by ultraviolet light induced polymerization. The hydrogel was alternately immersed in a cold (5 °C) and hot deionized water (ca. 70 °C) for 10 minutes. The purification step was repeated three times to remove unreacted monomers. The hydrogel taken out from the hot deionized water was quickly immersed in a 50 mg/ml LiCl solution and left to stand for 24 hours. Finally, CLP-LiCl AWH was obtained by freeze-drying the obtained hydrogel for 8 hours.

---

## 1.2 Structural Characterizations

X-ray photoelectron spectroscopy (XPS) was used to analyse the structure and composition of the samples by Thermo ESCALAB Xi+ with Al Ag source. The XPS spectra were calibrated through the standard C1s peak at 284.6 eV. Morphological characterization was characterized by scanning electron microscopy (SEM, FEI, Apreo 2S, America). UV-VIS spectra in the range of 200-1300 nm were recorded by a spectrophotometer (UV-2600, Shimadzu, Japan, BaSO<sub>4</sub> was used as a reflectance standard).

## 1.3 Measurements of solar-driven steam generation

The experimental setup consists of four parts: a light source, an analytical balance, an infrared (IR) camera, and the SSG device. A 1 kW m<sup>-2</sup> Xe lamp with an AM1.5 filter was used as the light source to simulate the sunlight. The analytical balance was used to record the changes in mass over time during the evaporation process. An infrared imager was used to record the real-time temperature. The test was carried out in the laboratory, and the room temperature was about 24 °C. For seawater desalination, the seawater was collected from the Yellow Sea of China.

## 2. Supplementary Figures

### 2.1 Microscopic observation of the RGO

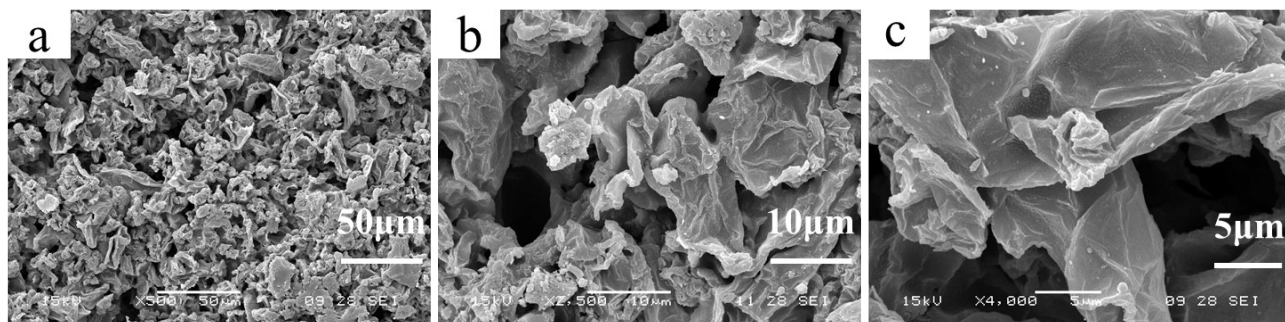


Figure S1. SEM images showing the microscopic structure of the RGO.

## 2.2 Functional groups on the RGO investigated by FTIR

The FTIR spectrum shows three main functional group. The peaks at 3300 nm, 1650 nm and 1100 nm correspond to C-H, C-C and C-O, respectively.

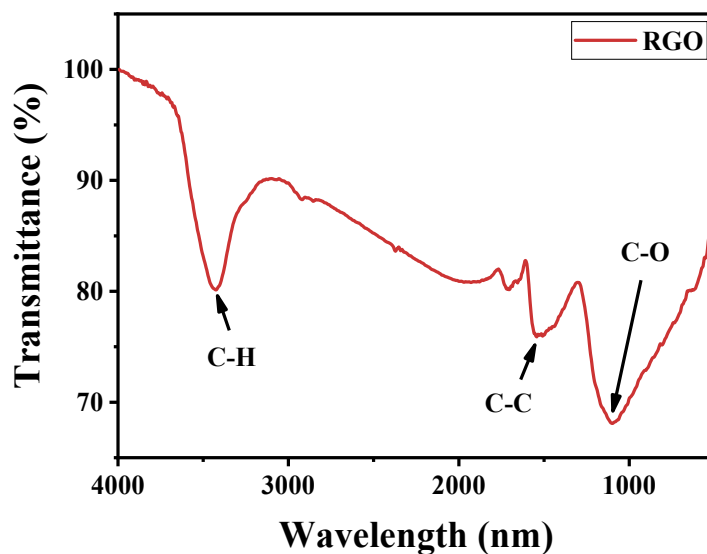


Figure S2. FTIR spectrum of the RGO.

## 2.3 Structure of the RGO investigated by XRD

Figure S3 shows the XRD pattern of RGO. A broad diffraction band can be observed at  $23^\circ$ , indicating that the carbon structure is amorphous and GO is effectively reduced.

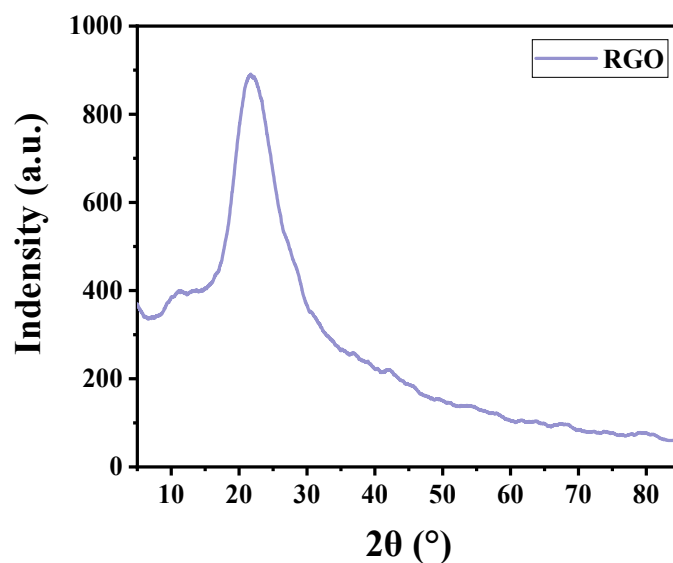


Figure S3. XRD pattern of the RGO.

---

## 2.4 More Explanation on the Relationship between Evaporation Area and Evaporation Rate

Supposing the evaporator can be well wetted, the evaporation rate can be significantly increased by enlarging the dark evaporation area due to the enhanced extraction of energy from the ambient environment. As shown in Figure S4, for the bundle, the irradiated surface area is  $S_{ir} = \pi R^2$  and the dark evaporation surface area is  $S_{dk} = 2\pi RH$ , where R is the radius of the bundle, and H is the height.  $S_{dk}$  increases with H, thus, the evaporator with largest height shows the highest water evaporation rate. And the ratio between dark and irradiated surface area is  $k = \frac{2\pi RH}{\pi R^2} = \frac{H}{R}$ . When the height keeps constant, the relative dark surface area increases as the radius decreases.

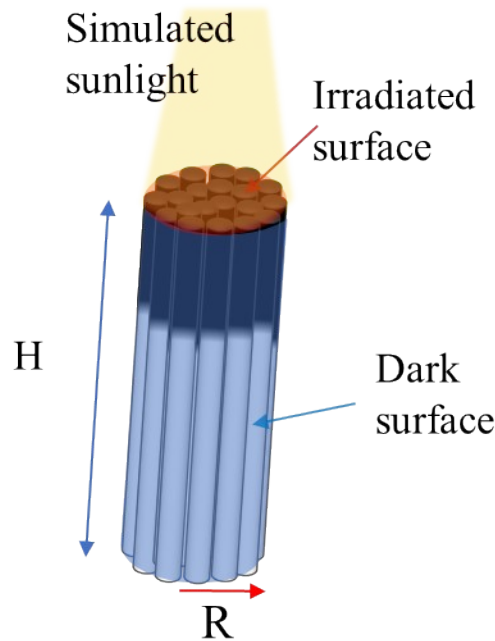


Figure S4. Schematic diagram illustrating the irradiated and dark surfaces of the RGO bundles.

## 2.5 Structure improvement

The specific surface area is further improved by dissociating the bundle into separated scrolls and reducing the radius of a single scroll. The masses of RGO on the two kinds of scrolls are measured. The RGO coating amounts are about 0.23 and 0.25 g for the scrolls with radii of 2.75 and 2.25 mm, respectively.

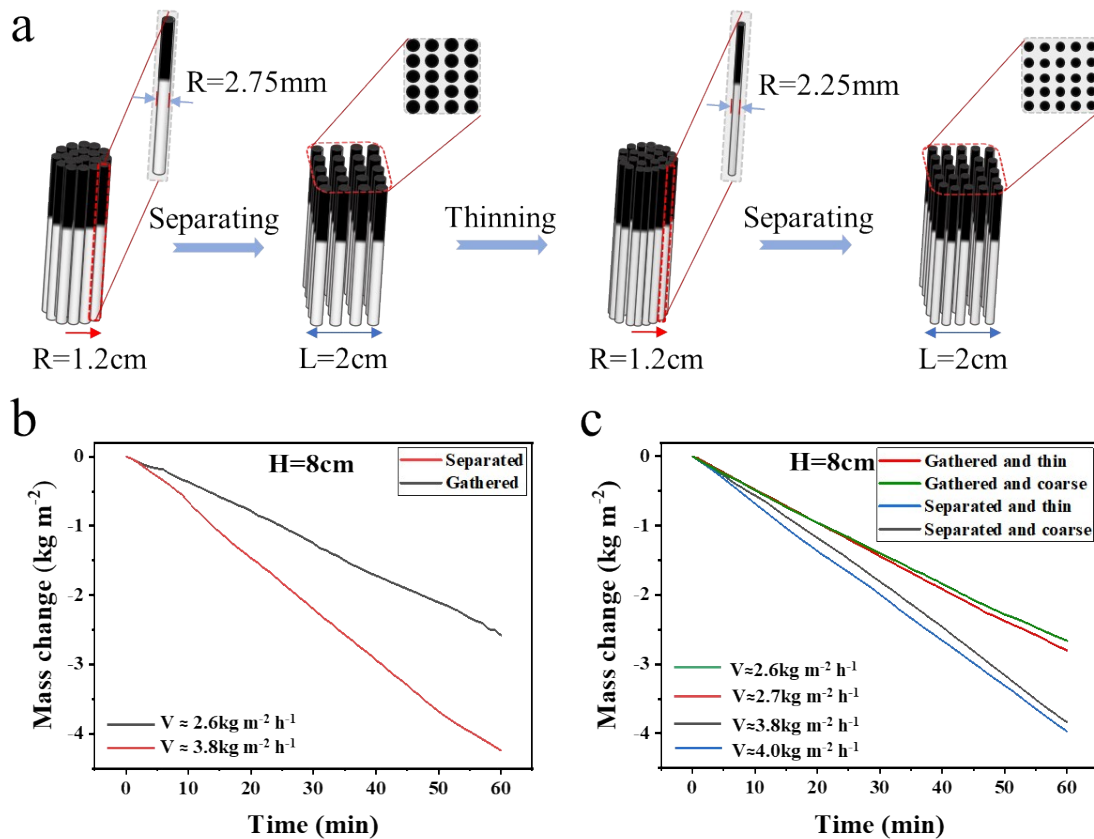


Figure S5. a) The specific surface area was improved by separating the evaporator into separate scrolls and reducing the radius of scrolls. b) Taking the evaporator with  $R=1.2\text{ cm}$  and  $H=8\text{ cm}$  as an example, comparison of the water evaporation rates by the separated and gathered RGO

## 2.6 Performance comparison of the bundles with RGO and without RGO

As Figure S6 shown, the performance of bundles with RGO are evidently higher than the control group due to the photothermal effect of RGO. It is noteworthy that the bundles without RGO show considerable water evaporation rate, which are even comparable to the performance of the 2D planar RGO membrane. These results further confirm the dark evaporation plays a very important role.

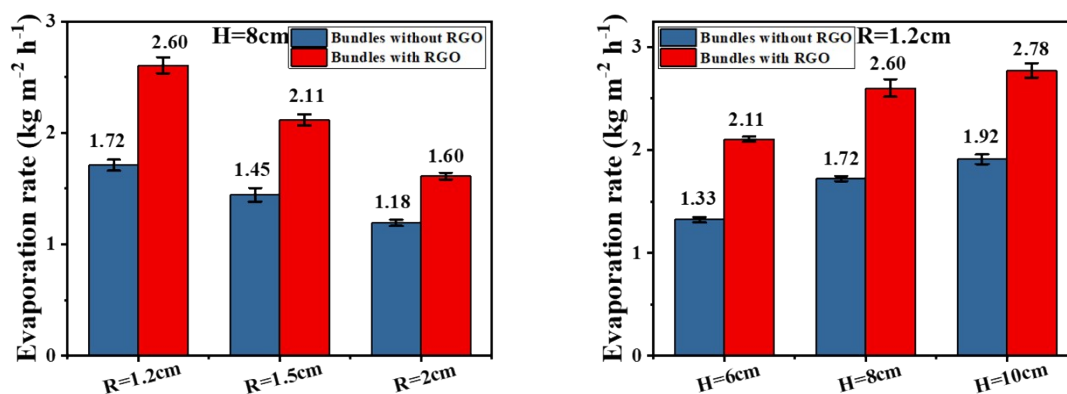


Figure S6. The performance of bundles without RGO are measured, which are compared with the RGO coated bundles.

## 2.7 Comparison of evaporation rate in irradiation and dark environments

Due to the existence of cold evaporation, the 3D evaporator also has a higher evaporation rate in a dark environment, and the evaporation rate increases with the increase of specific surface area.

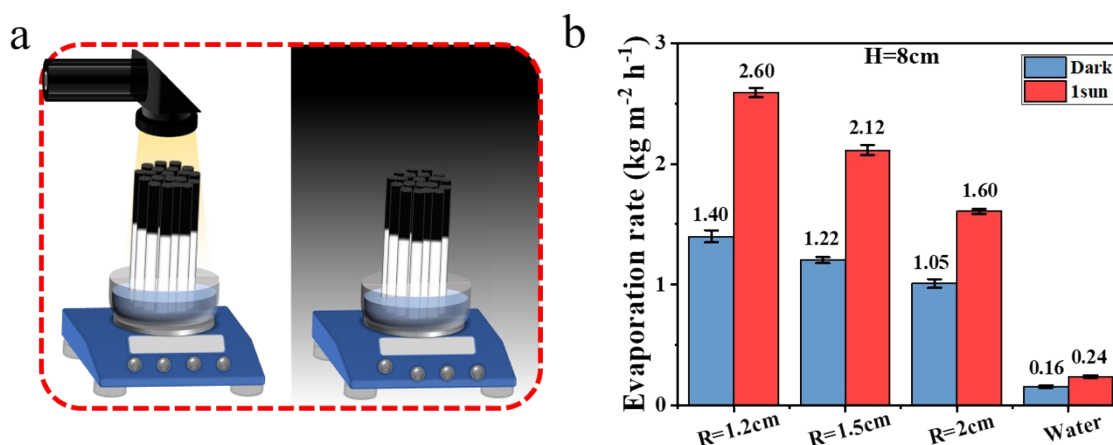


Figure S7. a) Schematic diagram of the water evaporation experiments conducted under 1 sun irradiation and dark environment. b) Comparison of evaporation rates under 1 sun irradiation and dark environment.

---

## 2.8 Solar steam generation process of 2D RGO membrane.

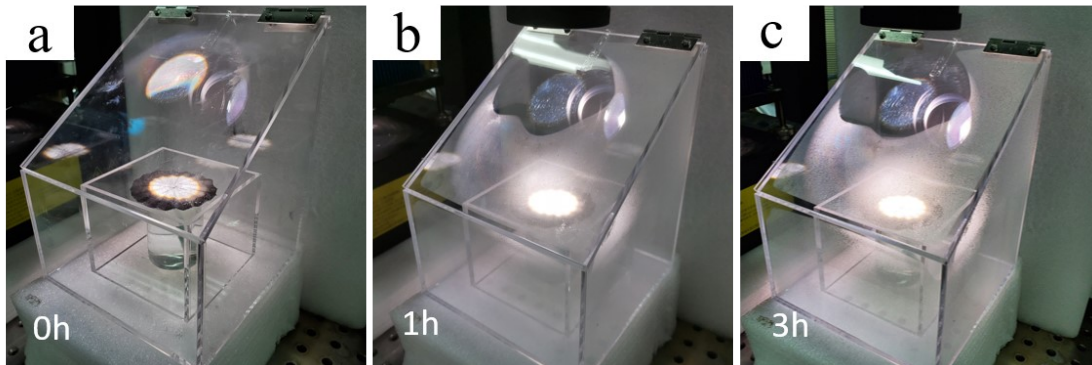


Figure S8. Accumulation of water mist in a closed chamber during continuous SSG by the 2D RGO membrane.

## 2.9 Moisture capturing experiment

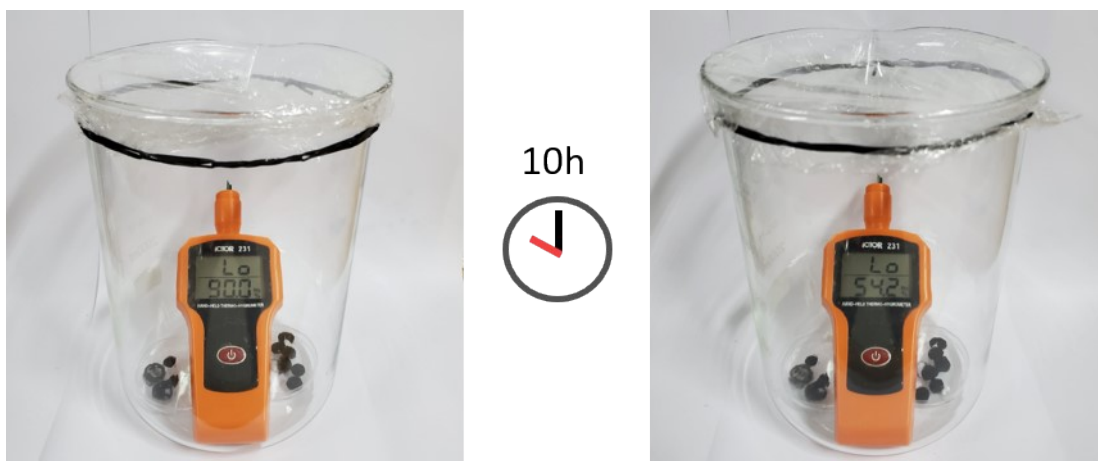


Figure S9. Hygroscopic experiment of the CLP-LiCl AWH in a closed chamber.

## 2.10 Chemical composition of the CLP-LiCl AWH investigated by XPS

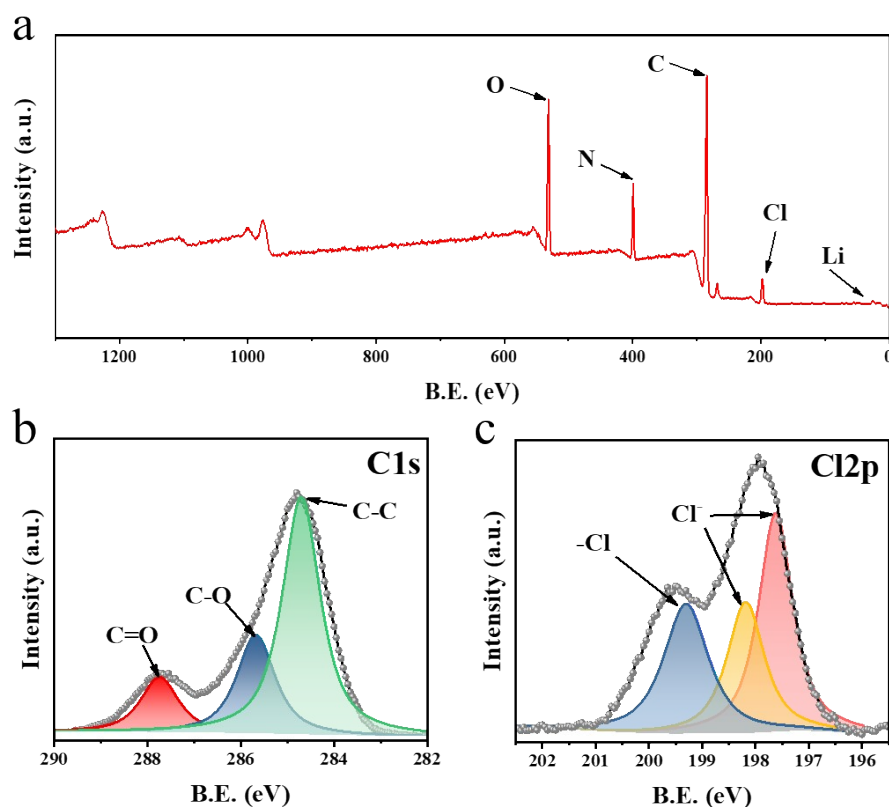


Figure S10. XPS spectra of the CLP-LiCl AWH. a) The XPS survey spectra shows five main elements including carbon, nitrogen, oxygen, chlorine and lithium. b) The high-resolution spectrum for C1s peak of CLP-LiCl AWH is deconvoluted into three components, the peaks at 284.8, 286.1 and 288.8 eV correspond to C-C, C-O and, C=O respectively. c) The high-resolution spectrum for Cl 2p peak of CLP-LiCl AWH is deconvoluted into three components, the peaks at 197.2, 198.3 and 200.2 eV correspond to Cl(-NH<sup>+</sup>-), Cl(H<sub>3</sub>O<sup>+</sup>) and covalent chlorine species (-Cl), respectively.

## 2.11 Microscopic observation of CLP-LiCl AWH

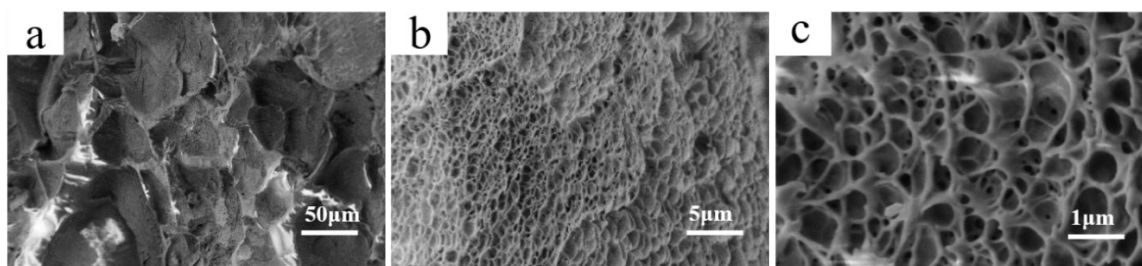


Figure S11. SEM image of the CLP-LiCl AWH.

## 2.12 Hydrophilicity test

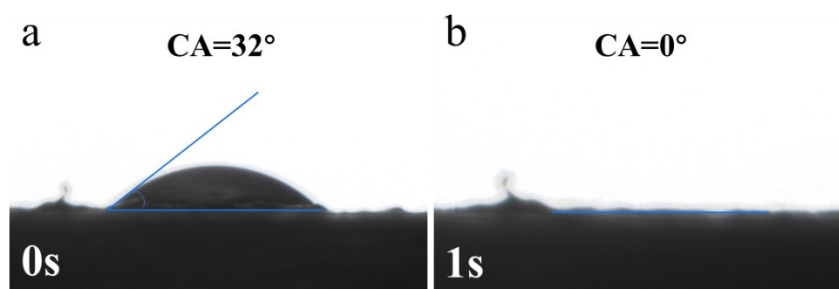


Figure S12. Water droplet contact angle of the CLP-LiCl AWH, demonstrating the super hydrophilic, which is beneficial to the adsorption of water vapor.

## 2.13 Thermogravimetric analysis (TGA)

Figure S13 shows TGA result of the CLP-LiCl AWH. With temperature increasing to 100 °C, the CLP-LiCl AWH shows a substantial weight loss, which is attributed to the evaporation of absorbed water.

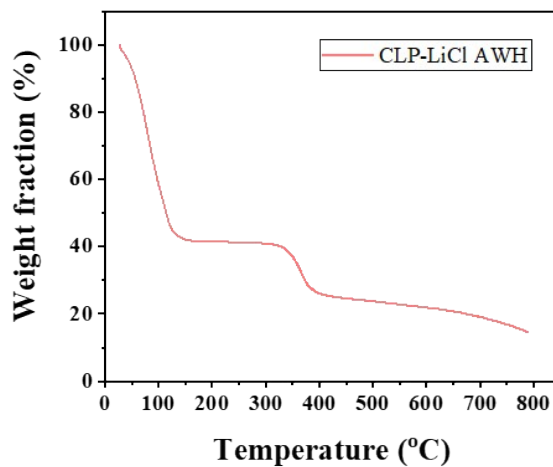


Figure S13. The TGA of the as-prepared CLP-LiCl AWH.

## 2.14 Cycling stability of moisture absorption–desorption

Figure S14 shows the CLP-LiCl AWH can maintain a stable water uptake rate after 10 cycles of absorption and desorption.

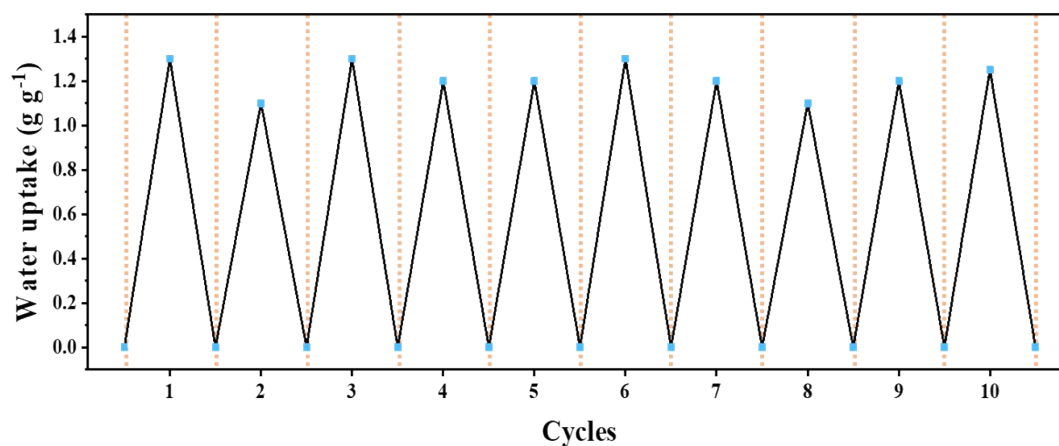


Figure S14. Cycling stability of moisture absorption–desorption of the CLP-LiCl AWH at 90% RH.

## 2.15 Water quality evaluation

Both the evaporator (3D RGO bundles) and CLP-LiCl AWH generate distilled water in the form of hot steam condensation, which means that Na<sup>+</sup>, Mg<sup>2+</sup>, Ca<sup>2+</sup> and K<sup>+</sup> in the raw seawater will not enter the distilled water, so the concentration of Na<sup>+</sup>, Mg<sup>2+</sup>, Ca<sup>2+</sup> and K<sup>+</sup> in the distilled water is much lower than the original Concentration in sea water.

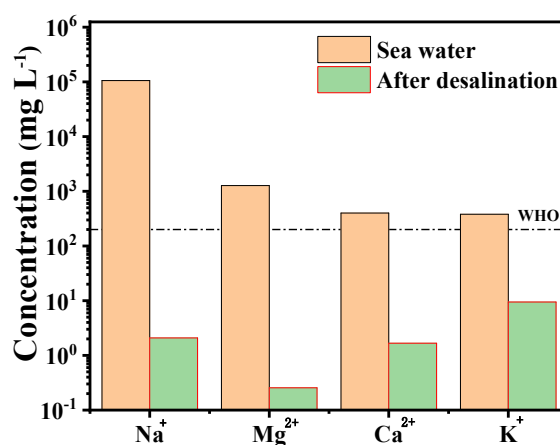


Figure S15. Ion concentrations of the seawater before and after desalination.

## 2.16 The effect of RGO side coating area on evaporation rate

The solar light mainly irradiates on the top surface, thus only top of the filter papers are covered by RGO. We would like to point out that RGO coated at the edge has negligible effect on the overall evaporation rate. As shown in Figure S16, the water evaporation rate almost keeps the same, when the RGO coating length changes from 3 to 8 cm.

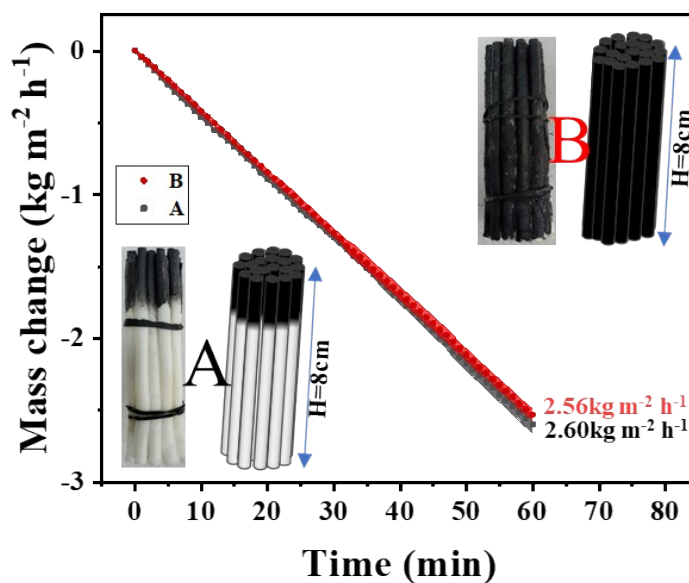


Figure S16. Water evaporation performances of two bundles with different RGO coating lengths. Insets: Photos and schemes of the two bundles.